Method based on the double sideband technique for the dynamic tracking of micrometric particles

Claudio Ramirez[1], Angel Lizana[1], Claudio Iemmi[2] and Juan Campos[1]

[1] Departamento de Física, Universitat Autònoma de Barcelona, Bellaterra, 08193, Spain
[2] Departamento de Física, FCEyN, Universidad de Buenos Aires—CONICET, Ciudad Universitaria, 1428, Buenos Aires, Argentina

E-mail: cramirezxp@gmail.com

Abstract

Digital holography (DH) methods are of interest in a large number of applications. Recently, the double sideband (DSB) technique was proposed, which is a DH based method that, by using double filtering, provides reconstructed images without distortions and is free of twin images by using an in-line configuration. In this work, we implement a method for the investigation of the mobility of particles based on the DSB technique. Particle holographic images obtained using the DSB method are processed with digital picture recognition methods, allowing us to accurately track the spatial position of particles. The dynamic nature of the method is achieved experimentally by using a spatial light modulator. The suitability of the proposed tracking method is validated by determining the trajectory and velocity described by glass microspheres in movement.

S Online supplementary data available from stacks.iop.org/JOPT/18/065603/mmedia

(Some figures may appear in colour only in the online journal)

1. Introduction

Over the last few decades, digital holography has arisen as a valuable tool for accurate and fast quantitative phase imaging applications. Nowadays, it is applied in different fields such as biology [1], optical metrology [2], imaging systems [3], among others.

The main architectures currently used to conduct imaging digital holography can be divided into two classes—those based on the original configuration proposed by Gabor [4] (in-line architectures [5, 6]), and those based on off-axis configurations [7–12], first proposed by Leith and Upatnieks [13, 14]. Both configurations present their own strengths and drawbacks. In-line configurations result in more robust and compact architectures, but typically undesired conjugate images are obtained in the reconstruction process. By contrast, off-axis architectures allow twin image removal, e.g., by some data processing at the Fourier plane, but they result in bulky systems that are more sensitive to vibrations and air flows.

In order to remove the conjugate images obtained with in-line configurations, different methods have been proposed. Most of them are based on phase shifting techniques that require multi-frame acquisition [15]. In this way, they are somewhat inappropriate for application to dynamic processes such as tracking of particles in a fluid or micro-organisms and live cells in a medium. Bryngdahl and Lohmann [16] proposed the single sideband (SSB) method, which is an interesting alternative to be applied in the study of dynamic processes with in-line configurations. In this technique half of

the complex valued frequencies of an object are removed at the Fourier plane and the other half are filtered during the reconstruction process. By following this approach, although the influence of the conjugate image is avoided, the object reconstruction appears distorted to certain extent because part of the information is lost in the process. To overcome this problem, we recently proposed the double sideband (DSB) method [17], which, by means of double filtering, is able to remove the twin image as well as to compensate for the above-stated distortions. The optical system used to implement the DSB method is based on a spatial light modulator (SLM), which acts as a double shutter, combined with two coupled charged devices (CCDs). This architecture allows us to carry out the double filtering instantaneously, so that the DSB method arises as a nice alternative for application to dynamic processes.

Different holographic methods are currently used for three dimensional profiling and tracking of particles [18]. In this work, we propose and test a method for the investigation of the mobility of particles by using the DSB method. Thus, all the benefits related to the DSB method (i.e. a dynamic technique providing reconstructed objects without twin images and image distortions) are also present in the tracking process. Object images obtained by means of the DSB technique are analyzed according to different digital reconstruction criteria—the Tamura coefficient [19], the entropy criterion [20, 21], the Gini index [22] and the analysis amplitude criterion [23]. In this paper, these criteria are compared and the best option is used to accurately determine the z coordinate of particles. In addition, to fully determine the three dimensional spatial position of the particle, once the z position is established, the transversal coordinates of the particle are also obtained through mass center calculations. Finally, by controlling the refresh rate of the CCDs used for data acquisition, the time elapsed between two consecutive frames (i.e. between two different spatial positions of the particle) allows us to calculate the instantaneous velocity of the particle. The experimental device is tested by measuring glass microspheres in motion, providing the interest for the technique to be applied to the tracking of micrometric particles.

The outline of this work is as follows. In section 2 we present a review of the mathematical foundations of the DSB technique for completeness. Next, in section 3, we describe different digital image recognition methods able to determine the best focused plane for a particle in motion (i.e. its actual position in the z axis). In addition, an approximation, based on mass center calculations, is used to establish the transversal coordinates of the particle. Afterwards, in section 4 the experimental results obtained when implementing the proposed method are provided. A discussion of the most suitable digital image recognition method (from the ones revised in this paper) is included. Also the experimental position and velocity of microspheres in motion are calculated as a function of time for a particular experiment. Finally, the main conclusions of this study are summarized in section 5.

2. Double sideband technique

Let us to start by summarizing the DSB technique proposed in [17]. The in-line configuration used to apply the DSB method is sketched in figure 1.

A laser beam is spatially filtered (SF) and then collimated by the convergent lens L1. The beam illuminates an object composed of two particles placed at two different planes labeled as P1 and P2. The incident beam (plane waves) is diffracted by the object and its corresponding Fourier spectrum is obtained at the focal plane of the convergent lens L2 (i.e. solid lines in figure 1). Moreover, the L2 lens simultaneously images an intermediate plane point onto the CCD cameras 1 and 2 (dashed lines in figure 1).

At the Fourier plane, the DSB filtering is performed. In our case we used a parallel aligned liquid crystal display (PA-LCD) that, in combination with two linear analyzers (LP2 and LP3 in figure 1), acts as a double shutter. In fact, the PA-LCD can be modeled as a linear variable phase plate oriented at 0 degrees whose retardance depends on the applied voltage [24]. We apply two different voltages to the two halves of the display, setting a retardance of $\delta_1 = 0$ degrees to one half and of $\delta_2 = 180$ degrees to the other half. Thus, if the PA-LCD is illuminated with linearly polarized light at 45 degrees of the laboratory vertical (by properly orienting the linear polarizer LP1), this polarization is conserved when passes through the first PA-LCD half ($\delta_1 = 0$ degrees) but it is rotated 90 degrees (i.e. it becomes linearly oriented at 135 degrees) when the light passes through the second display half ($\delta_2 = 180$ degrees). Afterwards, the wave front is divided at the beam-splitter (B-S) and later projected onto the LP2 and LP3 analyzers. These two linear analyzers are orthogonally oriented one to each other, namely, at 45 degrees and at 135 degrees. Under this configuration, the PA-LCD, together with LP2 and LP3, simultaneously act as upper and lower sideband filters, configuring the DSB filter.

Under this scenario, let us denote as $U_0(x, y)$ the complex value of the electric field at the CCD$_1$ and CCD$_2$ cameras if there were no filter at the Fourier plane. By assuming that we are dealing with an almost transparent object we can write:

$$U_0(x, y) = 1 + \Delta U_0(x, y), \qquad (1)$$

where ΔU_0 represents the contribution of the light diffracted by the particles. In this situation, the amplitude distribution at the Fourier plane can be calculated by Fourier transforming equation (1), leading to:

$$\tilde{U}_o(\mu, \nu) = \delta(\mu, \nu) + \Delta \tilde{U}_o(\mu, \nu), \qquad (2)$$

where δ denotes the Dirac delta function.

Due to the effect of the DSB filter at the Fourier plane, some frequencies of the object spectrum are blocked. In particular, whereas the frequencies $\mu < 0$ are blocked for the CCD1 optical arm, the frequencies $\mu > 0$ are blocked for the CCD2 optical arm. In this situation, the intensity distribution recorded at the CCD1 and CCD2 cameras are respectively
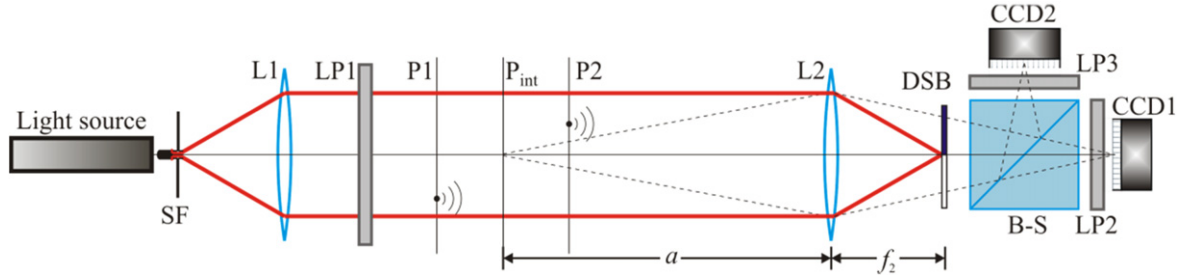
Figure 1. In-line optical architecture used to implement the DSB technique.

given by [17],

$$|U^+_{CCD1}|^2 \approx \frac{1}{4} + \underbrace{\frac{1}{2}\int_0^\infty \mathrm{d}\mu \int_{-\infty}^\infty \Delta\tilde{U}_o(\mu, \nu)e^{i2\pi(\mu x + \nu y)}\mathrm{d}\nu}_{\mathrm{A}^+}$$
$$+ \underbrace{\frac{1}{2}\int_{-\infty}^0 \mathrm{d}\mu \int_{-\infty}^\infty \Delta\tilde{U}_o^*(-\mu, -\nu)e^{i2\pi(\mu x + \nu y)}\mathrm{d}\nu}_{\mathrm{B}^+}, \quad (3)$$

$$|U^-_{CCD2}|^2 \approx \frac{1}{4} + \underbrace{\frac{1}{2}\int_{-\infty}^0 \mathrm{d}\mu \int_{-\infty}^\infty \Delta\tilde{U}_o(\mu, \nu)e^{i2\pi(\mu x + \nu y)}\mathrm{d}\nu}_{\mathrm{A}^-}$$
$$+ \underbrace{\frac{1}{2}\int_0^\infty \mathrm{d}\mu \int_{-\infty}^\infty \Delta\tilde{U}_o^*(-\mu, -\nu)e^{i2\pi(\mu x + \nu y)}\mathrm{d}\nu}_{\mathrm{B}^-}, \quad (4)$$

where the asterisk * denotes complex conjugation.

Note that whereas the second term (A^+) in equation (3) only contains frequencies $\mu \geqslant 0$, the third term (B^+) only contains frequencies $\mu \leqslant 0$. Analogously, whereas the second term (A^-) in equation (4) only contains frequencies $\mu \leqslant 0$, the third term (B^-) only contains frequencies $\mu \geqslant 0$. The image of the object under test can be retrieved from the information encoded in the terms (A^+) and (A^-). Nevertheless, the terms (B^+) and (B^-), which are related to the object conjugated wave, may degrade the final object reconstruction, so they must be deleted. Therefore, we digitally calculate the Fourier transform of the intensities given by equations (3) and (4) and frequencies $\mu \leqslant 0$ (related to the B^+ term) and $\mu \geqslant 0$ (related to the B^- term) are removed. Once this filtering at the Fourier space is applied, and by properly applying the inverse Fourier transform, equations (3) and (4) become respectively,

$$|U^+_{CCD}|^2_- = \frac{1}{4} + \frac{1}{2}\int_0^\infty \mathrm{d}\mu \int_{-\infty}^\infty \Delta\tilde{U}_o(\mu, \nu)e^{i2\pi(\mu x + \nu y)}\mathrm{d}\nu, \quad (5)$$

$$|U^-_{CCD}|^2_+ = \frac{1}{4} + \frac{1}{2}\int_{-\infty}^0 \mathrm{d}\mu \int_{-\infty}^\infty \Delta\tilde{U}_o(\mu, \nu)e^{i2\pi(\mu x + \nu y)}\mathrm{d}\nu, \quad (6)$$

where the subscripts $(-)$ and $(+)$ indicate that frequencies $\mu \leqslant 0$ and $\mu \geqslant 0$ have been removed.

Finally, by adding equations (5) and (6) we obtain:

$$I_{ccd}(x, y) = |U^+_{CCD}|^2_- + |U^-_{CCD}|^2_+$$
$$= \frac{1}{2} + \frac{1}{2}\int_0^\infty \mathrm{d}\mu \int_{-\infty}^\infty \Delta\tilde{U}_o(\mu, \nu)e^{i2\pi(\mu x + \nu y)}\mathrm{d}\nu$$
$$+ \frac{1}{2}\int_{-\infty}^0 \mathrm{d}\mu \int_{-\infty}^\infty \Delta\tilde{U}_o(\mu, \nu)e^{i2\pi(\mu x + \nu y)}\mathrm{d}\nu$$
$$= \frac{1}{2}U_o(x, y). \quad (7)$$

In this way the full complex amplitude, without the contribution of unwanted conjugate waves, is obtained. From this information, the wave front can be reconstructed at any arbitrary position by using some diffraction integral equation. In our case, we have used the Rayleigh–Sommerfeld diffraction equation [25], which is given by,

$$O(x, y, z) = \iint \tilde{I}_{ccd}(\mu, \nu)$$
$$\times \exp\left\{i\frac{2\pi}{\lambda}z[1 - \lambda^2(\nu^2 + \mu^2)]^{1/2}\right\}$$
$$\times \exp\{i2\pi(x\mu + y\nu)\}\mathrm{d}\nu\mathrm{d}\mu, \quad (8)$$

where $\tilde{I}_{ccd}(\mu, \nu)$ is the Fourier transform of $I_{ccd}(x, y)$ in equation (7).

3. Digital image recognition methods

The DSB technique is optimal for the reconstruction of the complex amplitude of an object located at different planes in depth, as it provides some advantages when compared with other existing methods. In addition, as the object reconstruction can be performed as a function of time (only limited by the CCD camera refresh rate), the method can be applied for dynamic applications, such as for the tracking of microscopic objects in motion.

The goal of this paper is to provide an efficient method suitable to determine the three dimensional position and velocity of particles as a function of time. Let us start by determining the z position of an isolated particle for a given instant of time. Note that an arbitrary plane perpendicular to the axial direction can be obtained according to equation (8). From all those possible transversal planes, we are interested in determining the best focused image of the particle, meaning to find the actual position of the particle in the z axis. To this

aim, different methods for digital image recognition can be applied [19–23, 26]. For the sake of clarity, some of those approaches are described in this section, i.e. the Tamura coefficient (section 3.1), the entropy criterion (3.2), the Gini index (3.3) and the amplitude analysis criterion (3.4). Note that in a forthcoming section, those criteria are experimentally tested to discern the most suitable approach for our purposes. Finally, once the z position is determined by the selected digital image recognition method, mass center calculations can be applied to the 'best focused' images, allowing us to also determine the transversal coordinates of the particles (see section 3.5).

3.1. The Tamura coefficient

In [19], Tamura *et al* proposed efficient processing methods for image recognition that are based on conditions specified in terms of human beings, i.e. mathematical processes highly correlated with statistical data of human observations. In this sense, they propose different textural specifications such as: coarse versus fine, high contrast versus low contrast, directional versus non-directional, line-like versus blob-like, regular versus irregular, rough versus smooth, among others. The mathematical expressions defined to evaluate the stated specifications have proved to efficiently determine the textural features of a widespread number of image patterns [19, 27]. However, in the case under examination, we are dealing with much more simple image patterns. In particular, as we work with spherical micrometric particles, object images are related to a black spot (more or less focused depending on the evaluated z) together with a light background. Therefore, only contrast is enough to achieve a good estimation of the best focused plane. Thus, in this work we use the mathematical expressions derived in [28], but adapted in such a way that only the contrast features are considered.

Let $I(i, j)$ be the image of an isolated particle for a given z position. The evaluated mean intensity for all the pixels in the image can be calculated as

$$\bar{I} = \frac{\sum_{i=1}^{m}\sum_{j=1}^{n} I(i, j)}{m \times n}, \tag{9}$$

where m and n are, respectively, the number of rows and columns of the image.

Once the mean intensity $\bar{I}$ of the region of interest (ROI) image is calculated, the standard deviation of the whole image is calculated according to,

$$\sigma(I) = \sqrt{\frac{1}{(m \times n) - 1}\sum_{i=1}^{m}\sum_{j=1}^{n}[I(i, j) - \bar{I}]^2}. \tag{10}$$

In our case of interest (the image of a micrometric particle), the reconstructed image for the best focused plane leads to the highest value of $\bar{I}$ (equation (9)). This is because, for the best focused plane, only a very small region of pixels (black spot) is contributing with null intensity values, whereas the rest of the image presents very similar (and high) intensity values. By contrast, as the particle image is defocused,

the smaller the value for $\bar{I}$ becomes. In this last case, the image of the particle (the spot) becomes blurred (defocused); this leads to low intensity values in a large area of the image, and thus to a lower mean intensity. Note that this argument is true when setting a ROI around a specific particle, because if the whole image is evaluated the total image energy is conserved. In addition to this, by following the same line of thought, we readily observe from equation (10) that the reconstructed image for the best focused plane leads to the minimum value for the image standard deviation $\sigma(I)$, whereas by going far from this plane, the standard deviation increases. Finally, this inverse behavior of $\bar{I}$ (equation (9)) and $\sigma(I)$ (equation (10)) as a function of z is used to define a merit function, this being based on their relative ratio [28],

$$TC = \sqrt{\frac{\sigma(I)}{\bar{I}}}, \tag{11}$$

where TC is the so-called Tamura coefficient and whose minimum value provides the z position of the particle best focused plane.

3.2. The entropy criterion

Another method used for refocusing images in digital holography is the self-entropy criterion [20, 21]. The entropy E of an image is an indicator of its degree of randomness. The entropy can be calculated from the histogram of the image, which shows the frequency of occurrence (or probability) of all the different gray levels present in the image. This situation can be mathematically written as follows:

$$E = -\sum_{n=1}^{N} P_n \log P_n, \tag{12}$$

where N is the number of gray levels and P_n is the number of pixels presenting the gray level n (i.e. the frequency of occurrence of the gray level n within the image).

Let us analyze the physical interpretation of the entropy criterion in our case of study. We readily see that, for a focused particle, the image randomness takes a minimum value. In fact, for an ideally focused image, only two gray levels are involved in the image—those corresponding to the black spot and the background. By contrast, as the image becomes blurred (defocused), the image randomness increases because the number of gray levels within the image becomes larger and thus the number of terms contributing in equation (12) grows. Therefore, the minimum value for E provides the z position of the best focused plane.

3.3. The Gini index

The Gini index (GI) constitutes a measure of the gray level sparsity in an image [22]. This means that an image presenting all the energy concentrated in a very small region leads to high values of the GI coefficient. By contrast, when an image presents energy being dispersed through the whole image, the GI coefficient becomes small.

Let f be a vector whose coefficients are the intensity values of the different N pixels of an image. Then, if the

elements of *f* are re-ordered from low to high values, we can build-up the vector $\underline{f} = [f(1),...,f(N)]$. Then, the Gini index can be written as follows [22],

$$GI(\underline{f}) = 1 - 2\sum_{k=1}^{N} \frac{f_k}{\|\underline{f}\|_{p=1}}\left(\frac{N-k+\frac{1}{2}}{N}\right), \qquad (13)$$

where $\|f\|_p = \sqrt[p]{|f(1)|^p+...+|f(N)|^p}$ is the norm and $p = 1$ in our case.

To interpret equation (13), let us study two different examples. First, let *f* describe an image with constant intensity *a*. This situation leads to $\underline{f} = [a,...,a]$ and $\|\underline{f}\|_{p=1} = N|a|$. Thus, equation (13) becomes,

$$\begin{aligned}GI(\underline{f}) &= 1 - 2\sum_{k=1}^{N} \frac{a}{Na}\left(\frac{N-k+\frac{1}{2}}{N}\right)\\ &= 1 - \frac{2}{N}\sum_{k=1}^{N}\left(1 - \frac{k}{N} + \frac{1}{2N}\right)\\ &= 1 - \frac{2}{N}\left(N - \frac{N+1}{2} + \frac{1}{2}\right) = 0.\end{aligned} \qquad (14)$$

Therefore, an image presenting a uniform gray level leads to a *GI* with minimum value. For the second example, let *f* describe an image where all the energy is concentrated in a single pixel. This leads to $\underline{f} = [0,0,...,a]$ and $\|\underline{f}\|_{p=1} = |a|$. Therefore, equation (13) becomes,

$$GI(\underline{f}) = 1 - 2\frac{a}{a}\left(\frac{N-N+\frac{1}{2}}{N}\right) = 1 - 2\left(\frac{1}{2N}\right) = 1 - \frac{1}{N}, \qquad (15)$$

and so for larger *N* values equation (15) tends to 1 and the *GI* coefficient takes a maximum value. Note that when dealing with the image of a particle, the best focused plane can be understood as the inverse situation rather than that defined for equation (15), and close to that in equation (14). Thus, we are interested in finding the minimum value for the *GI* coefficient.

3.4. The amplitude analysis criterion

Finally, we describe another criterion used for digital focusing processes. The main strength of this criterion is its easy interpretation, as it is only based on the total amplitude of the object reconstructed images [23]. In particular, it is calculated as the direct addition of the amplitude modulus corresponding to *N* image pixels. This expression reminds us of the denominator terms both in the Tamura and the Gini criteria and so the best focused plane is obtained for the highest summation. In particular, the amplitude analysis (*AA*) indicator is written as follows,

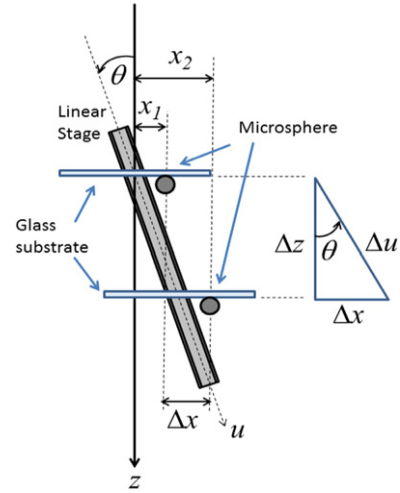$$AA = \sum_{k=0}^{N-1} a_k, \qquad (16)$$

Figure 2. Schematic diagram of the arrangement intended to simulate particles in motion.

where a_k is the amplitude modulus of the different pixels.

3.5. Transversal coordinates: mass center calculation

Once the *z* position of the particle is determined for a certain instant of time, according to some of the above-stated criteria, the transversal coordinates (*x*, *y*) of the particle must be obtained for such a plane. To this aim, we calculate the particle mass center from the image object obtained for the best focused plane. The expressions for the mass center of the particle in the *x* direction (*CMx*) and in the *y* direction (*CMy*), which have been adapted for intensities values, are respectively given by,

$$CMx = \frac{\sum_{i=1}^{m}\sum_{j}^{n} I(i,j) \times i}{I_M};$$
$$CMy = \frac{\sum_{i=1}^{m}\sum_{j=1}^{n} I(i,j) \times j}{I_M}, \qquad (17)$$

where *m* and *n* indicate the number of rows and columns in the image, *i* and *j* give the evaluated pixel coordinates and where I_M is the summation of the intensities throughout the whole image, given by,

$$I_M = \sum_{i=1}^{m}\sum_{j=1}^{n} I(i,j). \qquad (18)$$

4. Experimental results

To experimentally validate the proposed method, the set-up described in [9] was implemented in our laboratory. As an object we used soda lime glass microspheres with a nominal diameter of 90–106 μm (SLGMS −2.5 distributed by Cospheric). The microspheres were stuck to a glass substrate by electrostatic forces. Then, the glass substrate was mounted on a linear stage (8MT175—motorized linear stage
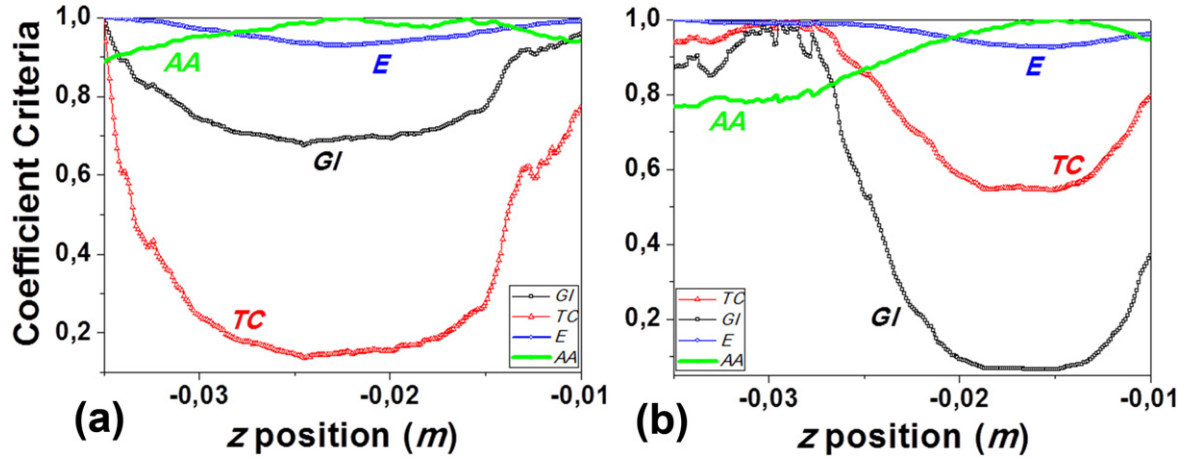
Figure 3. Tamura coefficient (*TC*; red triangles), Gini index (*GI*; black squares), entropy (*E*; blue circles) and amplitude analysis (*AA*; solid green line) values as a function of the *z* position for times: (a) t_1 and (b) t_2.

distributed by Standa) that can be electronically controlled. We set an angle θ between the optical axis of the system and the displacement direction $\vec{u}$ of the linear stage to simulate dynamic particles both with axial and lateral displacements (see figure 2). With this scheme, the displacement in the y direction is zero.

The linear stage movement started at a distance of -630 mm from the lens L2 ($f_2 = 300$ mm). While the linear stage is in movement, the two CCD cameras (see figure 1) are continuously recording intensity images. The cameras are Basler model PIA-1000-60gm (with a Truesense Imaging KAI-1020 CCD sensor) with a resolution of 1 MP and a pixel size of 7.4 μm. The CCD cameras are able to perform image acquisitions with a refresh rate of 60 frames per second at 1MP resolution. However, we set a lower refresh rate in our experiment (2 Hz) because it is selected to track the linear stage displacement velocity, which is not very high. Nevertheless, in the case of faster particle movements, the implemented method can be also applied, as it is only limited by the CCD refresh rate.

For the experimental alignment of the CCD cameras in the scheme shown in figure 1, the following procedure was followed. First, the system formed by the B-S and the CCD cameras (see figure 1) is roughly aligned in a first approximation by using an unexpanded laser beam (He-Ne, 633 nm) in a way that the light reflected on the two CCDs returns from the same path as the incoming light. Afterwards, as an object we use a resolution test (1951 USAF resolution test chart), this being imaged by L2 on the CCDs. Then, the position of the object is carefully corrected to obtain the best focusing image of the object for the CCD1. Afterwards, as the CCD2 is mounted on a *XYZ* linear translation stage, its position is corrected to obtain the best focusing image (with the same orientation and magnification as that of CCD1). Finally, a pixel-to-pixel alignment between the two CCD cameras is conducted by performing translations and rotations of the CCD2 in the transversal plane until the image of the resolution test falls in the same position in both cameras. Under this scenario, the intensity images recorded by the cameras,

Table 1. Best focused particle position (meters) provided by the different criteria for t_1 and t_2.

Criterion	t_1 z_{particle}	t_2 z_{particle}
TC	-0.0245	-0.0152
GI	-0.0245	-0.0152
E	-0.0224	-0.0150
AA	-0.0224	-0.0150

related to an intermediate plane (P_{int} in figure 1, at -600 mm from the L2), are treated by applying the DSB method explained above. So, for each instant of time, the transversal intensity distribution is obtained for any arbitrary z position, according to equation (8). At this stage, the z position of a specific microsphere is determined by calculating the best focused plane according to the different criteria explained in section 3. For calculations, the z step selected is 0.005 mm.

Note that for a set of particles in motion, different particles are in general at different z positions, so each best focused plane is different for each individual. In this situation, if the selected digital image recognition method is applied for all the particles at once, (i.e. starting from images including different particles), this can lead to incorrect results, providing some intermediate plane as the best solution. For this reason, a small (ROI) is set to the specific particle under study. In this situation, the particle of interest is tracked through the whole set of original images obtained for different z, which leads to a new set of object images of reduced dimension in which the particle is already isolated. In particular, we acquire intensity images of 1000×1000 pixels, whereas the ROI selected to track individual microspheres is 80×80 pixels. These ROI-based images as a function of the z position are the actual images used to apply the different digital image recognition methods, which provides the best focused plane in terms of z position for the isolated particle.

To decide which one of the different criteria defined in section 3 is more suitable to our particular case, figure 3 shows
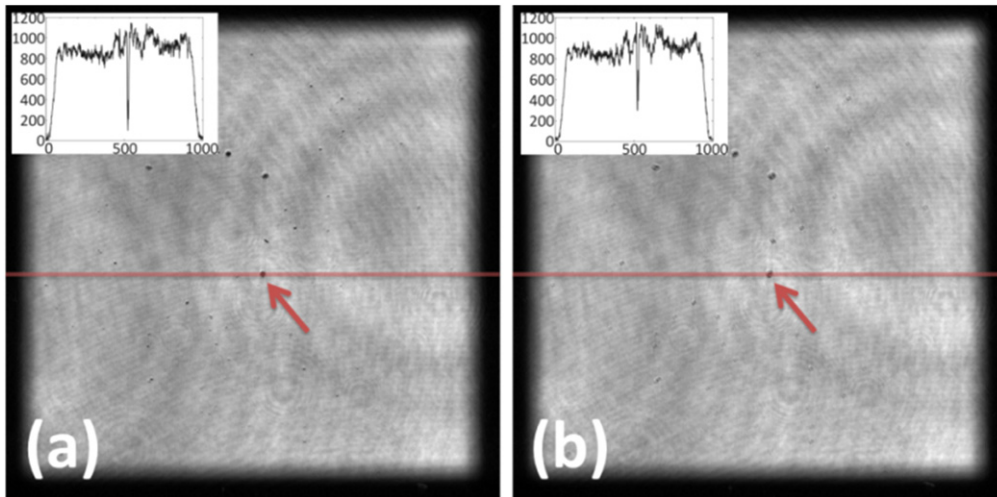
Figure 4. Best focused plane of the microsphere image obtained using the digital reconstruction criteria: (a) *TC* and *GI,* and (b) *E* and *AA*.

the variation of the different coefficients as a function of the z position. As explained in section 3, the minimum value for the Tamura coefficient (*TC*), the Gini index (*GI*) and entropy (*E*) gives the position of the best focused plane, whereas in the case of the amplitude analysis (*AA*) criteria, it is given by the maximum value. Such a representation is shown for two different instants of time, t_1 (figure 3(a)) and t_2 (figure 3(b)). The time elapsed between these two instants of time is 6 s, and thus the z position of the microsphere has changed. The best focused plane position $z_{particle}$ obtained with the different criteria for the t_1 and t_2 cases, is summarized in table 1. All the data are given in meters and they refer to the distance from the linear stage starting plane (−630 mm from L2).

Data in table 1 show that the *TC* and *GI* criteria give the same solution for the best focused plane, both for the t_1 and t_2 cases. The same situation is observed for the *E* and *AA* criteria. This can be understood by noticing the mathematical similarities between the expressions for the *TC* and *GI* criteria, as well as for the *E* and *AA* criteria (see section 3). However, between the solutions provided by the *TC–GI* criteria and those given by the *E–AA* criteria, although they are very close, we observe some small differences (i.e. 2.1 mm for t_1 and 0.2 mm for t_2). To choose which method is the most suitable in our particular case, we directly compare the reconstructed image of the best focused plane obtained using the *TC–GI* criteria ($z = -0.0245$ m) and using the *E–AA* criteria ($z = -0.0224$ m), for the t_1 case. Results are provided in figure 4(a) for the *TC–GI* criteria and in figure 4(b) for the *E–AA* criteria.

Just by conducting a visual comparison of the microsphere reconstructed images in figure 4, we observe that the *TC–GI* criteria lead to better results than the *E–AA* criteria in terms of particle focusing. Note that the specific particle tracked is marked with a red arrow in figure 4. For the sake of clarity, in the insets of figure 4, we also provide the cross-section related to the horizontal red line. This intensity information highlights the suitability of the *TC–GI* approaches, as the intensity valley related to the focused image particle is significantly deeper than for the *E–AA* cases.
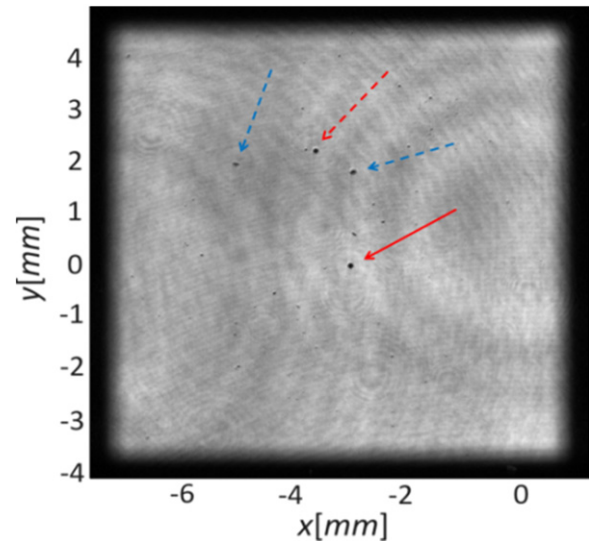

Figure 5. Video of the tracked microspheres (avaliable at stacks.iop. org/JOPT/18/065603/mmedia).

In addition, this fact has been tested for different times (i.e. for different particle positions in the z axis), and in all the cases we have obtained analogous results. For this reason, we can state that the *TC* and the *GI* criteria are the most suitable for our goal, i.e. for microsphere tracking. Therefore, from now on all the forthcoming studies will be based on calculations obtained using the Tamura coefficient and the Gini index. If a more accurate comparison between methods is of interest, a complete overview of refocusing criteria in digital holography can be found in [29].

Finally, once the best focused plane is obtained with the selected method, the corresponding x and y coordinates of the microsphere are calculated according to equation (17). At this stage, the spatial position of an individual microsphere is obtained for any instant of time. A video (based on $\sim 8 \times 8$ mm^2 images) is provided in figure 5, which compares the obtained microsphere images as a function of the time,
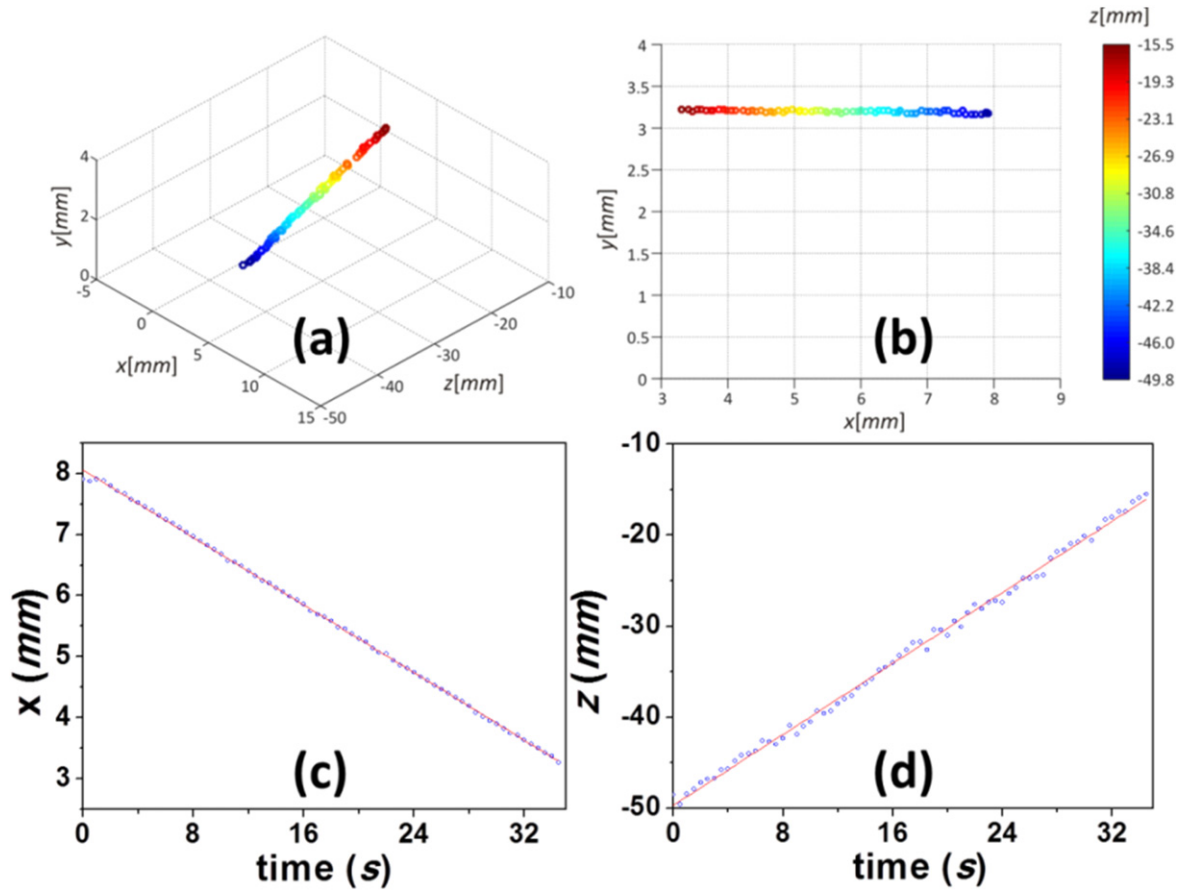
Figure 6. Spatial trajectory of the microsphere determined using the *GI* criterion: (a) 3D visualization; (b) *X–Y* plane view; (c) *x* position as a function of time; (d) *z* position as a function of time.

when no refocusing method is applied (left-hand side) and when our refocusing technique is used (right-hand side).

The chosen sphere to be tracked is that one marked with a continuous red arrow in figure 5. When our tracking technique is not applied (left-hand side video) the sphere is always defocused because the particle is always far from the intermediate plane (the one imaged by L2 onto the CCD cameras, figure 1). In turn, when applying our proposed technique (right-hand side video), the sphere is always focused independently of its spatial position. Other spheres are focalized as well because they are close to the selected one (marked in figure 5 with dashed arrows).

As the video in figure 5 results in a 2D representation of the microsphere movement, the *z* displacement of the particle is not noticeably observed. Thus, the calculated trajectory in the 3D space of the tracked microsphere is represented in figure 6(a) (the data shown is based on the *GI* criterion). The *X–Y* plane view is also provided in figure 6(b). For the sake of clarity, the *x* and *z* coordinates are also represented as a function of the time in figures 6(c) and (d), respectively (the *y* coordinate is not shown because it is almost zero, i.e. $\sim 10^{-6}$ meters). As the velocity of the linear stage is approximately constant—its magnitude can be set with the control software provided by the fabricant—the spatial coordinates of the particle follow a linear behavior as a function of time.

The accuracy of our method is limited by the fluctuations of the experimental data around the linear regressions shown in figures 6(c) and (d). The regressions are given by $x(t) = 8.056 - 0.138t$ (regression coefficient $R^2 = 0.999$) and $z(t) = -49.667 + 0.975t$ ($R^2 = 0.9968$) in figures 6(c) and (d), respectively. Thus, in order to find the bounds in our measurements we have calculated the absolute error between the experimental coordinates $x_{\exp}$ and $z_{\exp}$, which are obtained using our method, and the *x* and *z* values obtained from the linear regressions in figure 6 for the same instants of time. The obtained results are given in figure 7. For comparison, we also provide data based on the *TC* criterion. The obtained linear regressions in this last case were: $x(t) = 7.998 - 0.138t$ ($R^2 = 0.999$) and $z(t) = -49.317 + 0.963t$ ($R^2 = 0.999$).

The errors obtained by using the *TC* (empty blue squares) and *GI* (solid red circles) criteria are very close one to each other, as was expected from the data provided in figure 3 and table 1. We obtain a very good estimation for the particle *x* position (figure 7(a)), with errors lower than 0.15 mm both for the *GI* and *TC* cases. Larger errors are obtained for the determination of the *z* position (figure 7(b)), this being better determined by using the *GI* criterion (maximum error of 1 mm). A more detailed comparison between the *TC* and *GI* criteria can be found in [30]. As previously discussed, the *z* position was determined by searching the minimum of the *GI*
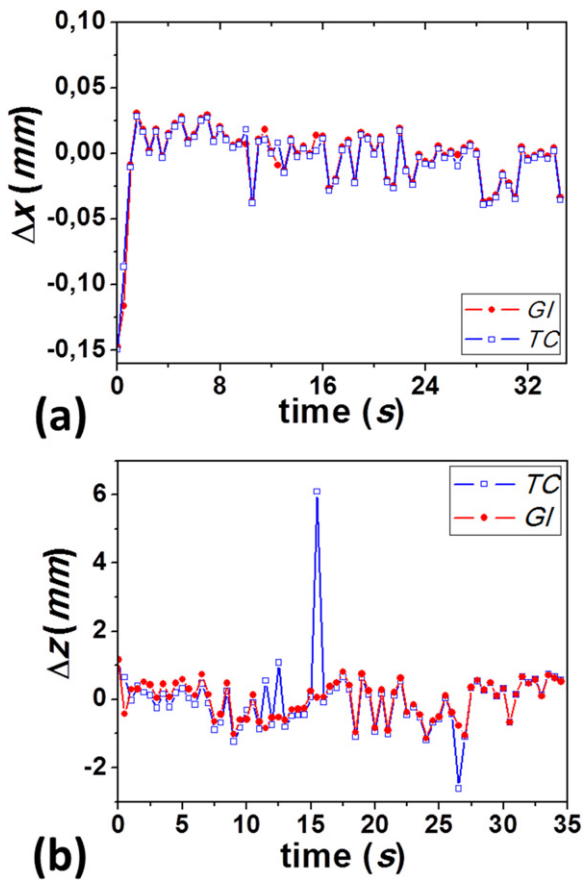
Figure 7. Absolute error for the particle position as a function of time: (a) *x* coordinate and (b) *z* coordinate.
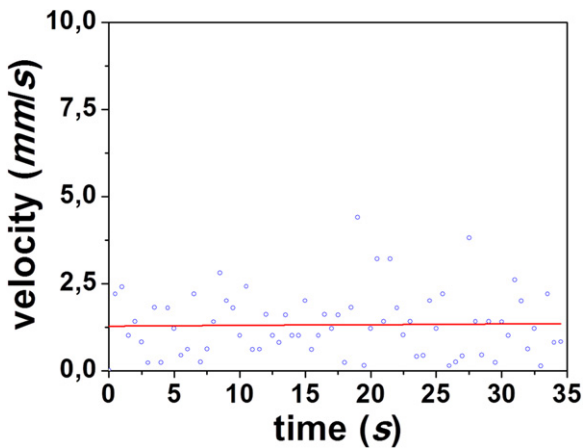

Figure 8. Microsphere velocity as a function of time.

and *TC* functions. However, experimental constraints, such as the numerical aperture (*NA*) of the beam, the beam-splitter accurate azimuthal positioning or noise present in the interferograms, affect the minimum shape of the *GI–TC* functions, which imposes a limitation on the *z* determination (see figure 3). In particular, the larger the valley width of the minimum, the bigger the *z* error becomes. If an accuracy lower than 1 mm is required for the *z* determination, different

strategies can be adapted such as using a larger *NA*, setting an intensity threshold on the intensity patterns, optimizing the size of the ROI, reducing interferential effects related to reflections on the optical elements in the set-up, etc.

Finally, from the calculated microsphere spatial coordinates, and by knowing the time elapsed between two consecutive frames, the velocity of the microsphere in the $\vec{u}$ direction (see figure 2) is also determined as a function of time. The obtained results (based on the *GI* criterion) are given in figure 8.

As expected, because the linear stage is set to a constant velocity the microsphere velocity is also constant, as provided by the slope of the linear regression conducted on the data (i.e. $f(t) = 1.283 + 0.002t$). To estimate the dispersion of the velocity measurements as a function of time, the standard deviation σ is also calculated from data in figure 8 ($\sigma = 0.903$ (mm s^{-1})).

5. Conclusions

In this work we use a digital holographic method for the investigation of the mobility of micrometric particles using the DSB technique. This method provides instantaneous reconstructed images of the analyzed object without the influence of twin images as well as without the typical deformations associated to the SSB technique.

To determine the instantaneous position of the particle in the axial direction, the images provided by the DSB method are treated according to different digital image reconstruction criteria: the Tamura coefficient, the entropy criterion, the Gini index and the amplitude analysis criterion. We have proved that for our particular application, the dynamic tracking of micrometric particles, the Tamura coefficient and the Gini index (*GI*) provide the best results in terms of particle focusing in the *z* direction, the *GI* criterion leading to the smallest errors. Once the *z* coordinate is determined, the transversal coordinates are obtained from mass center calculations. From this data, and by knowing the time elapsed between two consecutive frames, the velocity of the particle can be also calculated.

The method has been experimentally validated by tracking glass microspheres in motion, showing the suitability of this technique to be applied to dynamic processes, such as those involving particles in a fluid or micro-organisms and live cells in a media. As a proof of concept, the tracking of a glass microsphere in motion is provided in video format. In addition, quantitative information of the analyzed microsphere is also provided by calculating its spatial position (errors <0.15 mm for *x* and <1 mm for *z*, for the intervals $\Delta x \simeq 5$ mm and $\Delta z \simeq 35$ mm, respectively) and velocity (errors <0.9 mm s^{-1}) as a function of time.

References

[1] Carl D, Kemper B, Wernicke G and Bally G V 2004 Parameter-optimized digital holographic microscope for high-resolution living-cell analysis *Appl. Opt.* **43** 6536–44

[2] Proll K P, Nivet J M, Körner K and Tiziani H J 2003 Microscopic three-dimensional topometry with ferroelectric liquid-crystal-on-silicon displays *Appl. Opt.* **42** 1773–8

[3] Khare K, Ali P T S and Joseph J 2013 Single shot high resolution digital holography *Opt. Express* **21** 2581–91

[4] Gabor D 1948 A new microscopic principle *Nature* **4098** 777–8

[5] Moon I, DaneshPanah M, Javidi B and Stern A 2009 Automated three-dimensional identification and tracking of micro/nanobiological organisms by computational holographic microscopy *Proc. IEEE* **97** 990–1010

[6] DaneshPanah M and Javidi B 2007 Tracking biological microorganisms in sequence of 3D holographic microscopy images *Opt. Express* **15** 10761–6

[7] Tajahuerce E, Matoba O and Javidi B 2001 Shift-invariant three-dimensional object recognition by means of digital holography *Appl. Opt.* **40** 3877–86

[8] Javidi B and Tajahuerce E 2000 Three-dimensional object recognition by use of digital holography *Opt. Lett.* **25** 610–2

[9] Moon I and Javidi B 2006 Three-dimensional identification of stem cells by computational holographic imaging *J. R. Soc. Interface* **4** 305–13

[10] Yeom S, Moon I and Javidi B 2006 Real-time 3D sensing, visualization and recognition of dynamic biological microorganisms *Proc. IEEE* **94** 550–66

[11] Shin D, Daneshpanah M, Anand A and Javidi B 2010 Optofluidic system for three-dimensional sensing and identification of micro-organisms with digital holographic microscopy *Opt. Lett.* **35** 4066–8

[12] Javidi B, Moon I, Yeom S and Carapezza E 2005 Three-dimensional imaging and recognition of microorganism using single-exposure on-line (SEOL) digital holography *Opt. Express* **13** 4492–506

[13] Leith E N and Upatnieks J 1962 Reconstructed wavefronts and communication theory *J. Opt. Soc. Am.* **52** 1123–30

[14] Leith E N, Upatnieks J and Haines K A 1965 Microscopy by wavefront reconstruction *J. Opt. Soc. Am.* **55** 981–6

[15] Yamaguchi I and Zhang T 1997 Phase-shifting digital holography *Opt. Lett.* **22** 1268–70

[16] Bryngdahl O and Lohmann A 1968 Single-sideband holography *J. Opt. Soc. Am.* **58** 620–4

[17] Ramirez C, Lizana A, Iemmi C and Campos J 2015 Inline digital holographic movie based on a double-sideband filter *Opt. Lett.* **40** 4142–5

[18] Yu X, Hong J, Liu C and Kim M K 2014 Review of digital holographic microscopy for three-dimensional profiling and tracking *Opt. Eng.* **53** 112306

[19] Tamura H, Mori S and Yamawaki T 1978 Textural features corresponding to visual perception *IEEE Trans. Syst. Man Cybern.* **SMC-8** 460–73

[20] Thum C 1984 Measurement of the entropy of an image with application to image focusing *Opt. Acta* **31** 203–11

[21] Gillespie J and King R A 1989 The use of self-entropy as a focus measure in digital holography *Pattern Recognit. Lett.* **9** 19–25

[22] Zonoobi D, Kassim A A and Venkatesh Y V 2011 Gini index as sparsity measure for signal reconstruction from compressive samples *IEEE J. Sel. Top. Signal Process.* **5** 927–32

[23] Dubois F, Schockaert C, Callens N and Yourassowsky C 2006 Focus plane detection criteria in digital holography microscopy by amplitude analysis *Opt. Express* **14** 5895–908

[24] Lizana A, Marquez A, Lobato L, Rodange Y, Moreno I, Iemmi C and Campos J 2010 The minimum Euclidean distance principle applied to improve the modulation diffraction efficiency in digitally controlled spatial light modulators *Opt. Express* **18** 10581–93

[25] Pedrini G, Osten W and Zhang Y 2005 Wave-front reconstruction from a sequence of interferograms recorded at different planes *Opt. Lett.* **30** 833–5

[26] Latychevskaia T and Fink H W 2014 Holographic time-resolved particle tracking by means of three-dimensional volumetric deconvolution *Opt. Express* **22** 20994–1003

[27] Qi Y L 2009 A relevance feedback retrieval method based on Tamura texture *Proc. IEEE* **3** 174–7

[28] Memmolo P, Iannone M, Ventre M, Netti P A, Finizio A, Paturzo M and Ferraro P 2012 On the holographic 3D tracking of *in vitro* cells characterized by a highly-morphological change *Opt. Express* **20** 28485

[29] Memmolo P, Miccio L, Paturzo M, Di Caprio G, Coppola G, Netti P A and Ferraro P 2015 Recent advances in holographic 3D particle tracking *Adv. Opt. Photonics* **7** 713–55

[30] Memmolo P, Paturzo M, Javidi B, Netti P A and Ferraro P 2014 Refocusing criterion via sparsity measurements in digital holography *Opt. Lett.* **39** 4719–22